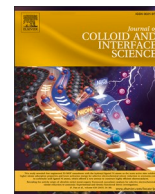


Contents lists available at [ScienceDirect](https://www.sciencedirect.com)

Journal of Colloid And Interface Science

journal homepage: www.elsevier.com/locate/jcis

Hollow-Structured N-doped carbon-embedded CoFe NanoAlloy for boosting activation of Monopersulfate: Engineered interface and heteroatom Doping-Induced enhancements

Tran Doan Trang^a, Jechan Lee^b, Wen-Da Oh^c, Eilhann Kwon^d, Haitao Wang^e, Yiu Fai Tsang^f, Venkata Subbaiah Munagapati^g, Hongta Yang^{h,*}, Wei-Hsin Chen^{i,j,k}, Kun-Yi Andrew Lin^{a,l,*}

^a Department of Environmental Engineering & Innovation and Development Center of Sustainable Agriculture, National Chung Hsing University, Taichung, Taiwan

^b Department of Global Smart City & School of Civil, Architectural Engineering, and Landscape Architecture, Sungkyunkwan University, Suwon, 16419, Republic of Korea

^c School of Chemical Sciences, Universiti Sains Malaysia, 11800 Penang, Malaysia

^d Department of earth resources and environmental engineering, Hanyang University, SeongDong-Gu, Seoul, Korea

^e Key Laboratory of Pollution Processes and Environmental Criteria, College of Environmental Science and Engineering, Nankai University, Tianjin 300071, China

^f Department of Science and Environmental Studies, The Education University of Hong Kong, Tai Po, New Territories 999077, Hong Kong

^g Research Centre for Soil & Water Resources and Natural Disaster Prevention (SWAN), National Yunlin University of Science and Technology, Douliou, Yunlin 64002, Taiwan

^h Department of Chemical Engineering, National Chung Hsing University, Taichung, Taiwan

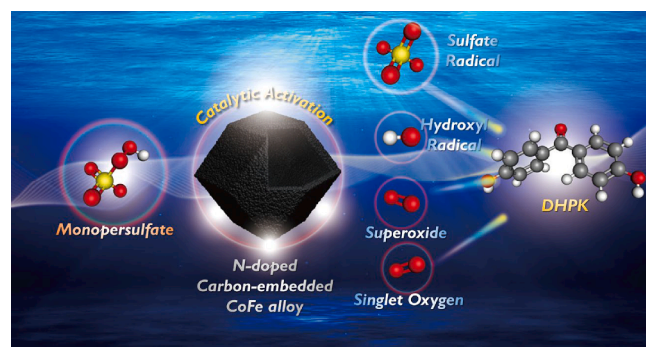
ⁱ Department of Aeronautics and Astronautics, National Cheng Kung University, Tainan 701, Taiwan

^j Research Center for Smart Sustainable Circular Economy, Tunghai University, Taichung 407, Taiwan

^k Department of Mechanical Engineering, National Chin-Yi University of Technology, Taichung 411, Taiwan

^l Institute of Analytical and Environmental Sciences, National Tsing Hua University, Hsinchu, Taiwan

GRAPHICAL ABSTRACT



ARTICLE INFO

Keywords:
Oxone
Sulfate radical

ABSTRACT

While transition metals are useful for activating monopersulfate (MPS) to degrade contaminants, bimetallic alloys exhibit stronger catalytic activities owing to several favorable effects. Therefore, even though Co is an efficient metal for MPS activation, CoFe alloys are even more promising heterogeneous catalysts for MPS

* Corresponding authors.

E-mail addresses: hyang@nchu.edu.tw (H. Yang), linky@nchu.edu.tw (K.-Y. Andrew Lin).

<https://doi.org/10.1016/j.jcis.2023.08.091>

Received 21 June 2023; Received in revised form 3 August 2023; Accepted 13 August 2023

Available online 14 August 2023

0021-9797/© 2023 Elsevier Inc. All rights reserved.

AOPs
MOFs
Alloy

activation. Immobilization/embedment of CoFe alloy nanoparticles (NPs) onto hetero-atom-doped carbon matrices appears as a practical strategy for evenly dispersing CoFe NPs and enhancing catalytic activities via interfacial synergies between CoFe and carbon. Herein, N-doped carbon-embedded CoFe alloy (NCCF) is fabricated here to exhibit a unique hollow-engineered nanostructure and the composition of CoFe alloy by using Co-ZIF as a precursor after the facile etching and Fe doping. The Fe dopant embeds CoFe alloy NPs into the hollow-structured N-doped carbon substrate, enabling NCCF to possess the higher mesoscale porosity, active N species as well as more superior electrochemical properties than its analogue without Fe dopants, carbon matrix-supported cobalt (NCCo). Thus, NCCF exhibits a considerably larger activity than NCCo and the benchmark catalyst, Co_3O_4 NP, for MPS activation to degrade an environmental hormone, dihydroxydiphenyl ketone (DHPK). Besides, NCCF + MPS shows an even lower activation energy for DHPK degradation than literatures, and retains its high efficiency for eliminating DHPK in different water media. DHPK degradation pathway and ecotoxicity assessment are unraveled based on the insights from the computational chemistry, demonstrating that DHPK degradation by NCCF + MPS did not result in the formation of toxic and highly toxic by-products. These features make NCCF a promising heterogeneous catalyst for MPS activation to degrade DHPK.

1. Introduction

Advanced oxidation processes (AOPs) are essential techniques for wastewater treatments to eliminate emerging contaminants. Traditionally, AOPs involve the production of reactive oxygen species (ROS) with high oxidation potentials for the decomposition of pollutants. While the Fenton's reaction would generate hydroxyl radicals ($\cdot\text{OH}$) to destroy organic contaminants, sulfate radical ($\text{SO}_4^{\cdot-}$)-based AOPs are gaining growing interest because $\text{SO}_4^{\cdot-}$ possesses a high oxidation power of 2.5–3.1 V, and $\text{SO}_4^{\cdot-}$ can be applied in a wider pH range with higher selectivity and longer half-lives [1–3], making $\text{SO}_4^{\cdot-}$ -based AOPs advantageous for treating refractory and toxic contaminants.

For obtaining $\text{SO}_4^{\cdot-}$, various commercial precursors are readily available, such as monopersulfate (MPS), which must be activated in order to rapidly liberate $\text{SO}_4^{\cdot-}$. Among numerous activation methods (such as heat, light irradiation, ultrasound, and catalysts) [4–7], heterogeneous catalysts are recognized as the most promising method for activating MPS, and transition metals (e.g., Co, Fe, Mn, Ni, etc.) are promising metals for activating MPS [2,3,8,9].

Although Co has been confirmed as the most efficient metal and numerous types of Co-bearing materials have been thoroughly developed for activating MPS, recent studies have found that bimetallic materials consisting of Co and another metal exhibit synergistic effects that boost catalytic activities [10,11]. Specifically, bimetallic alloys of Co and another metal could have even more advantageous properties, such

as increased catalytic activities due to the abundance of electrons and magnetism [12–15], and CoFe alloy appears to be an intriguing bimetallic catalyst for MPS activation [12,16,17] as Fe is one of the earth's most abundant elements.

However, direct use of CoFe alloy or other Co-bearing nanoparticles (NPs) may result in a number of issues, including NP agglomeration, difficult NP recovery, and rapid deactivation [18,19]. Therefore, immobilization or embedding CoFe alloy NPs in substrates is a practicable strategy. Since carbon materials are highly accessible and stable, carbonaceous substrates have been employed for supporting/embedding CoFe alloy NPs [20,21]. In addition, carbon substrates can be doped with heteroatoms (such as nitrogen) to increase electron transfer and catalytic activity by providing more reactive sites [22,23]. Thus, developing a hybrid catalyst for embedding CoFe alloy into N-doped carbon substrates would be advantageous for MPS activation in order to degrade refractory contaminants.

Despite the fact that most embedding of NPs onto carbon substrates can be accomplished through post-modifications, such a post-modification approach would inevitably confront problems, such as poor NP dispersion, NP aggregation, and low NP loading [24,25]. Utilizing templates that contain target components (i.e., metals and organics), followed by thermal treatments would be an even more advantageous method for fabricating such a hybrid catalyst. In particular, metal organic frameworks appear to be a compelling template due to their coordinated structures and incorporation of metal/organics

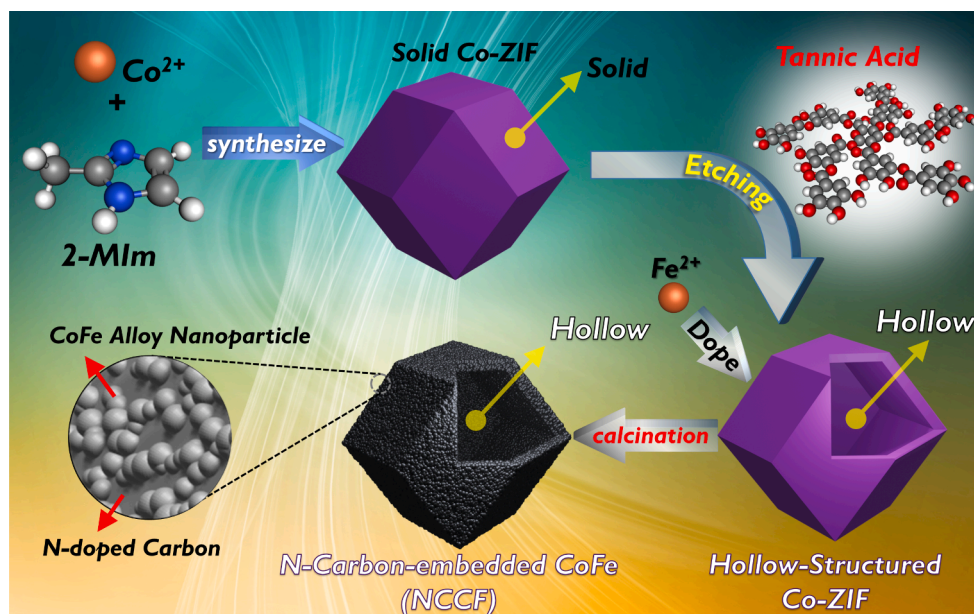


Fig. 1. Preparation scheme for NCCF.

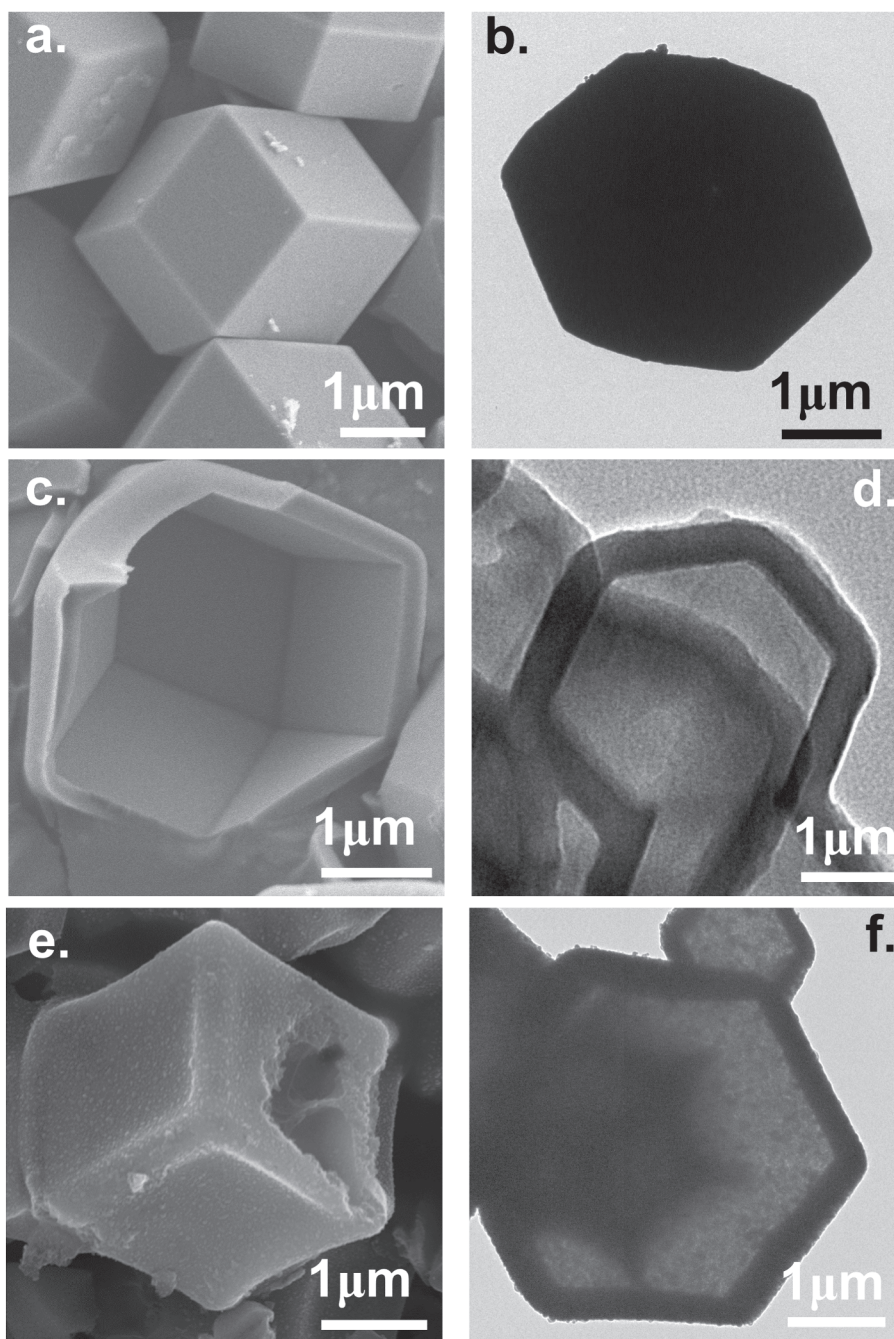


Fig. 2. Electronic microscopic images of (a-b) solid Co-ZIF; (c-d) hollow-structured Co-ZIF; and (e-f) *N*-doped carbon-supported CoFe (NCCF).

[26], and Co-ZIF would be an ideal template because imidazolate's ligand can be converted to *N*-doped carbon. The addition of Fe to Co-ZIF would result in the formation of CoFe alloy after direction carbonization.

On the other hand, despite the fact that Co-ZIF has polyhedral geometries and typical diameters of a few hundreds of nanometers, the derivative metal alloys would be difficult for accesses even after carbonization [27,28]. Therefore, we propose a straightforward and effective method for creating hollow Co-ZIF structures by carving the interior portion of Co-ZIF, formulating a box-like hollow morphology with thin layers. After depositing Fe onto such a “nanobox” and then carbonizing it, a thin *N*-doped carbon-embedded CoFe alloy (NCCF) would be produced. Such an NCCF consisting of CoFe ally NPs encapsulated on a well-defined *N*-doped carbon would be a promising

activator for MPS to degrade recalcitrant pollutants. Specifically, dihydroxydiphenyl ketone (DHPK) would be chosen as a representative emerging contaminant because DHPK is a widely used UV light stabilizer that is frequently applied to cosmetics, plastics, films, adhesives, and coatings. However, DHPK has been validated as an endocrine disruptor [29].

To investigate the catalytic activities of NCCF for removing emergent contaminants from polluted water, the degradation of DHPK by MPS activated by NCCF would be investigated. Importantly, a *N*-doped carbon-embedded cobalt (NCCo), which is an analogue to NCCF without Fe doping, would also be fabricated for direct comparison with NCCF in order to investigate the surface structure–property relationship of such hybrid materials. The corresponding degradation pathway of DHPK by NCCF + MPS would be investigated using both experimental analysis

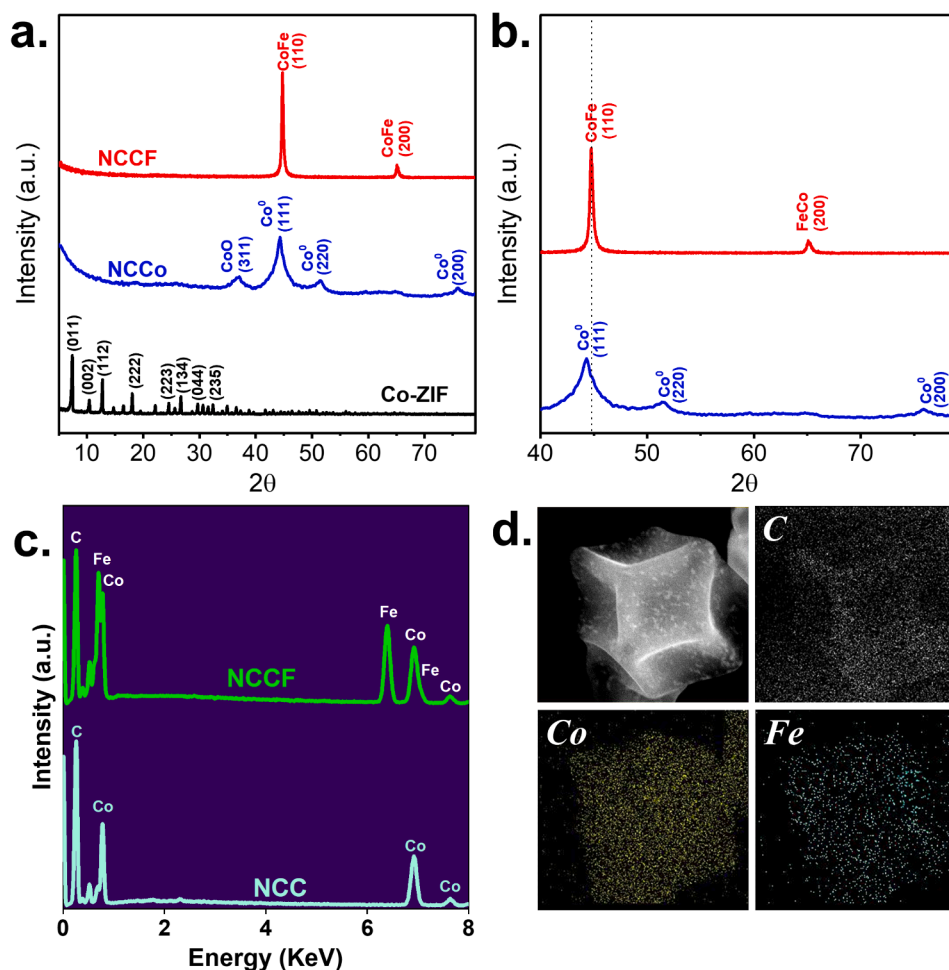


Fig. 3. (a–b) XRD patterns and (c) EDS of NCCF and NCCo; (d) mapping analysis of NCCF.

and computer-assisted research; the ecotoxicity of the possible intermediates would be also be assessed.

2. Experimental

The fabrication of NCCF was implemented as depicted in Fig. 1, and the detailed synthesis process, DHPK degradation by MPS, analytical procedures, and computational chemistry are provided in the supplementary material.

In order to quantify the degradation kinetics, the pseudo 1st order rate law would be utilized to calculate the observed rate constant, k :

$$\ln(C_t/C_0) = -kt \quad (1)$$

3. Results and discussion

3.1. Properties of NCCF

Morphologies and Compositional analyses

As NCCF was derived from Co-ZIF, the morphology of Co-ZIF was first determined, as depicted in Fig. 2(a), which revealed the typical rhombic dodecahedron with distinct faces and well-defined edges. The transmission image of Co-ZIF (Fig. 2(b)) demonstrates that the pure Co-ZIF was solid.

Moreover, Fig. 3(a) demonstrates that the XRD pattern of pure Co-ZIF corresponds well to the previously reported pattern [28,30,31], indicating that Co-ZIF had been synthesized.

Through post-treatment with tannic acid and doping with Fe^{2+} ,

followed by carbonization, the final product (Fig. 2(e)) retained the rhombic dodecahedral morphology; however, the faces of the final product were visibly roughened and adorned with numerous fine nanoparticles (NPs). Importantly, the original solid structure had been transformed into a porous structure with extremely thin outer layers, as evidenced through the fracture. The corresponding transmission image (Fig. 2(f)) confirmed that the solid texture of pristine Co-ZIF had vanished and been replaced by a hollow texture, with an outer layer whose thickness was approximately 200 ~ 400 nm.

The hollow structure was caused by tannic acid which possesses plentiful single bond OH groups and liberates free proton (H^+) to decompose the characteristic Co-N bonds [32]. Meanwhile, new N—H bonds and coordinated Co-tannic acid complex can be formed [33], converting the Co-ZIF coordination framework into a coordination network between Co^{2+} ions and tannic acid [32,33]. Those tannic acid and partial Co-tannic acid coordination compounds can easily attach on the surface, relieving the collapses of outer parts. Then, the hollow structure was then afforded by the continuous etching and re-coordination [32,33]. Thus, the XRD pattern of the tannic acid-etched Co-ZIF was noticeably changed and characteristic peaks of the pristine Co-ZIF were modified as shown in Fig. S1.

In addition, Fig. 2(e) reveals that the outermost layers of the final product were actually assembled by a large number of NPs. Through etching, doping, and carbonization, the Co-ZIF was transferred to another material, which displayed a distinct pattern from those of Co-ZIF (Fig. 3(a)). In particular, a few peaks were identified on 44.9° and 65.2°, that were attributed to CoFe alloy (JCPDS Card # 65–6829). The

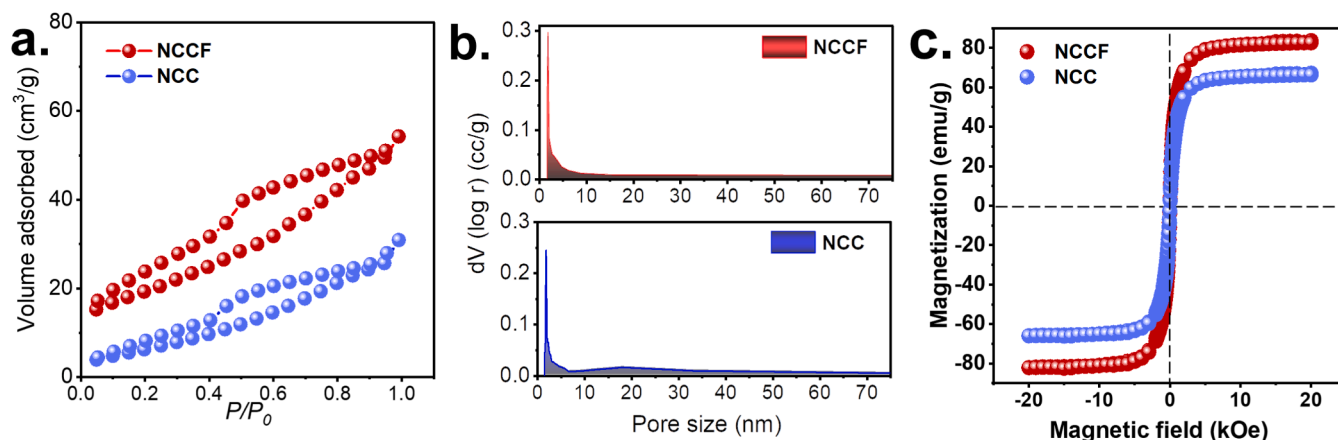


Fig. 4. (a) N₂ sorption isotherms, (b) pore size distributions, (c) saturation magnetization of NCCF and NCCO.

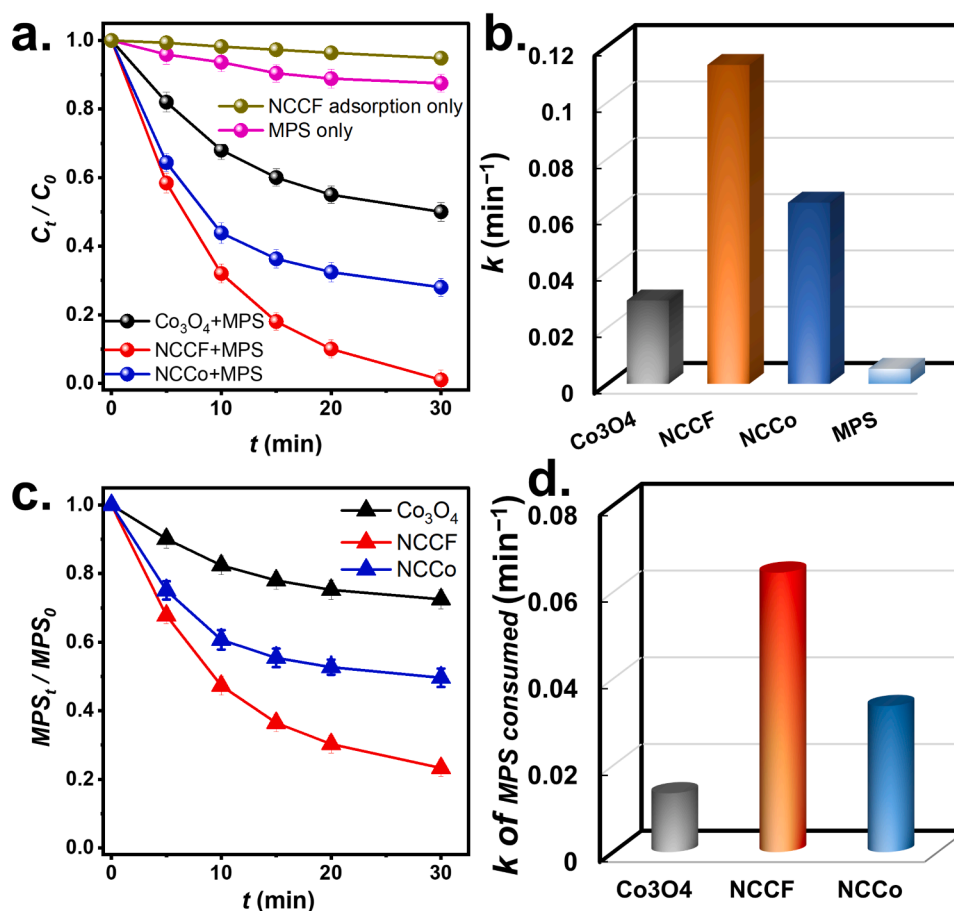


Fig. 5. (a) Comparison of degradation of DHPK and (b) corresponding rate constants of DHPK degradation; (c) comparison of MPS consumption and (d) rate constants of MPS consumption (Catalyst = 200 mg/L, MPS = 200 mg/L, T = 30 °C).

presence of CoFe alloy (Fig. 3(b)) confirmed that Fe was successfully inserted into the final product, and that the pure Co-ZIF had been transformed into a hybrid material composed of carbon and, more crucially, CoFe alloy. Fig. 3(c) further displays the EDS analysis of NCCF, in which only Co, Fe, C, and a minor fraction of N were obtained without other noticeable elements. Fig. 3(d) depicts the mapping analysis of NCCF, which reveals the uniform distribution of carbon, Fe, and Co throughout these NCCF, confirming that the etching and Fe doping were applied uniformly to Co-ZIF during the fabrication process.

On the other hand, an analog of NCCF was also synthesized without Fe²⁺ doping. Even without Fe²⁺ doping, the etching and carbonization treatment effectively converted Co-ZIF to a hollow-structured material, as shown in Fig. S2(a-b). Fig. 3(a) also illustrates the XRD pattern of NCCo, which was distinct from that of Co-ZIF, with a series of prominent peaks at 36.7°, 44.2°, 51.6°, and 75.6°. In particular, the signal at 36.7° could be attributed to CoO (JCPDS Card # 43–1004) due to the partial oxidation of Co⁰, whereas 44.2°, 51.6°, and 75.6° were ascribed to Co⁰ (JCPDS Card # 15–0806), resulting in the formation of N-doped carbon

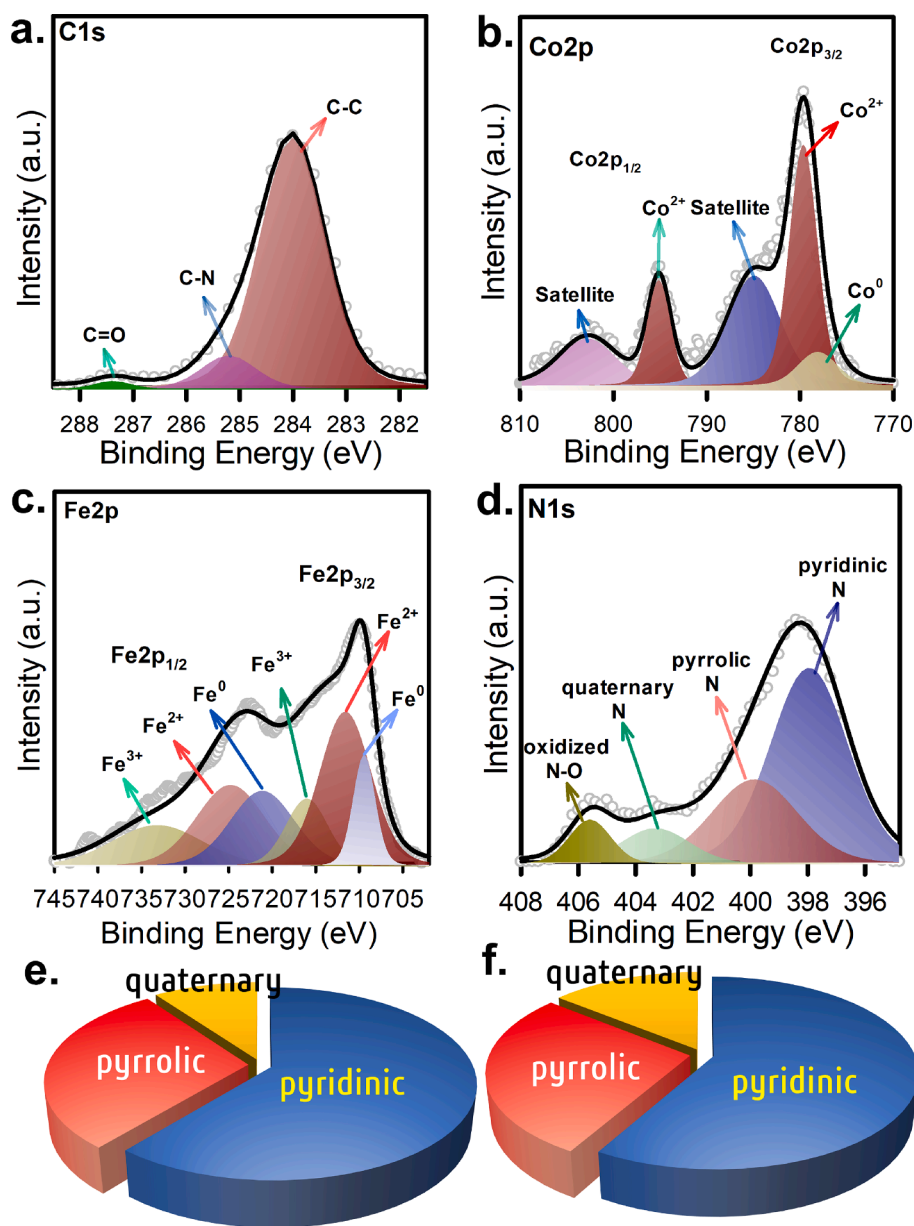


Fig. 6. (a-d). XPS analyses of NCCF; fractions of N species in (e) NCCF and (f) NCCo.

embedded Co (NCCo).

Textural properties

As NCCF exhibited a unique hollow structure with the embedment of NPs onto carbon substrates, its textural property was then further analyzed in Fig. 4(a), and the sorption curve could be classified as a type IV adsorption accompanied by a noticeable hysteresis, suggesting that NCCF was porous, especially mesoporous. The large hysteresis loop also suggested that the porous structures in NCCF was more complex possibly because differently-sized NPs of CoFe alloy were embedded into the carbon matrix, creating more pores. The presence of mesopores is confirmed by its pore distribution (Fig. 4(b)), which ranges from 2 to 75 nm. The relatively high N_2 sorption also enabled NCCF to show a high surface area as $68 \text{ m}^2/\text{g}$ and its pore volume was determined as 0.055 cc/g .

The sorption curve of NCCo was measured in Fig. 4(a). A relatively low N_2 sorption was achieved and the corresponding hysteresis loop was much smaller. Therefore, the surface area of NCCo was relatively lower as $26 \text{ m}^2/\text{g}$, and its pore volume was merely 0.045 cc/g , which was much lower than that of NCCF.

Since NCCF consisted of CoFe alloy, it has magnetic characteristics and hence it might be intriguing to explore the magnetic features of the NCCF. In Fig. 4(c), NCCF displayed a significant magnetization, and its saturation magnetization reached 82.5 emu/g , which was significantly higher than that of NCCo as 64.3 emu/g . The embedment of CoFe alloy allowed NCCF to manifest powerful magnetization, rendering it a material that can be readily recovered.

3.2. Degradation of DHPK by NCCF + MPS system

In Fig. 5(a), the elimination of DHPK by MPS activated by NCCF was evaluated. Due to the possibility that DHPK could be eliminated via adsorption, the adsorption of DHPK onto NCCF was investigated. In Fig. 5(a), the concentration of DHPK hardly changed in the presence of NCCF, indicating that DHPK could not be removed via adsorption. Using MPS alone, DHPK was only marginally eliminated in 30 min, demonstrating that MPS without activation was incapable of destroying DHPK effectively. However, when NCCF and MPS were combined, DHPK concentration decreased rapidly and was completely eliminated in 30

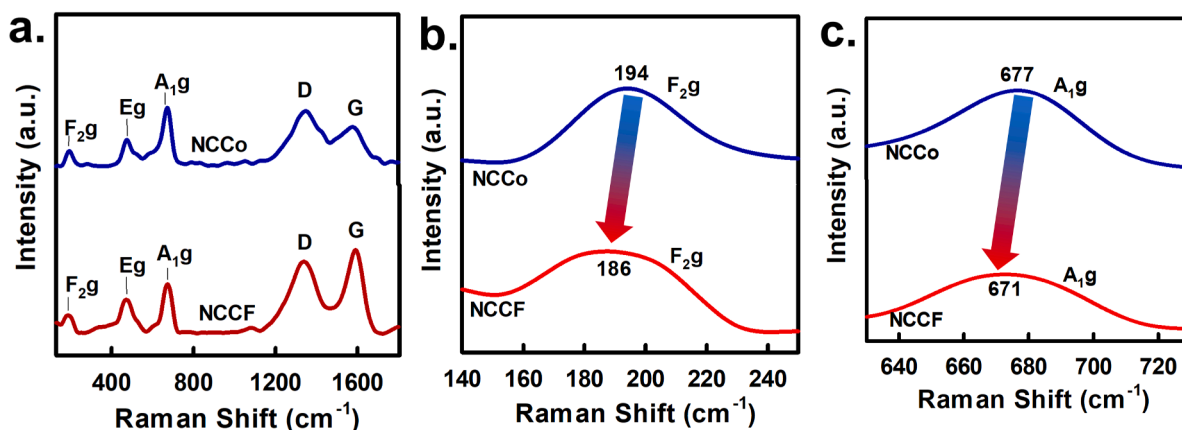


Fig. 7. (a). Full-survey Raman spectra of NCCF and NCCo; (b-c), regional Raman spectra of NCCF and NCCo; and (d) fractions of G and D bands in NCCF and NCCo.

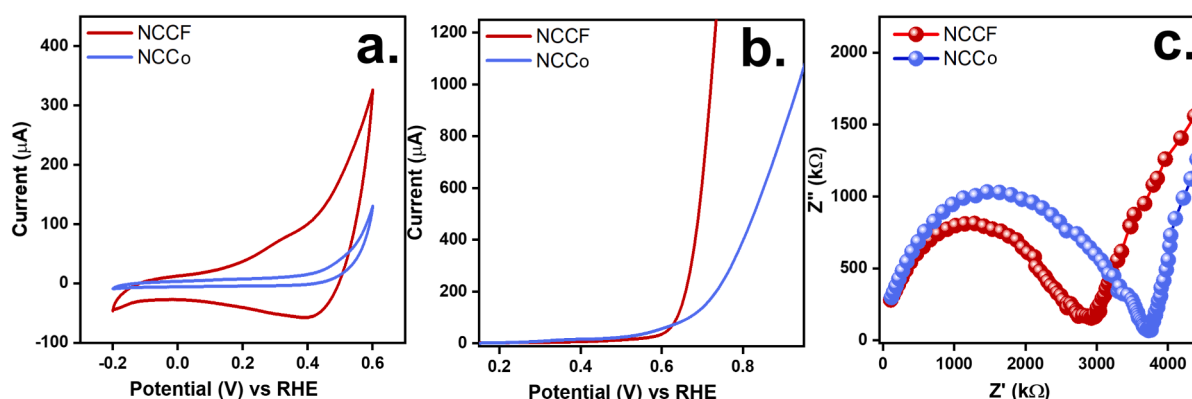


Fig. 8. Electrochemical properties of NCCF and NCCo: (a) CV curves, (b) LSV curves, (c) EIS Nyquist plots.

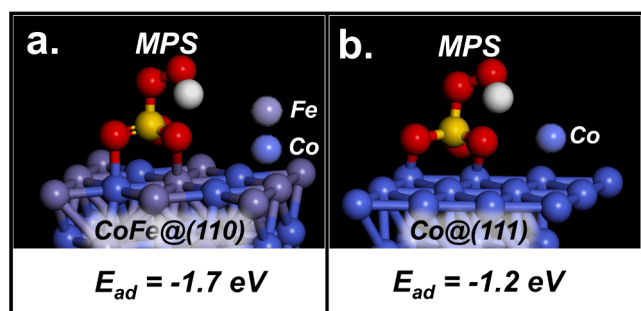


Fig. 9. DFT calculation: adsorption of MPS to (a) CoFe@110, and (b) Co@111.

min, indicating that NCCF could activate MPS to remove DHPK from water. Comparatively, Co₃O₄ NP (Fig. S3) and NCCo were also used to decompose MPS for the elimination of DHPK in Fig. 5(a). In 30 min, Co₃O₄ NP + MPS enabled C_t/C_0 to reach 0.63 (i.e., 37% of DHPK was removed), whereas NCCo + MPS resulted in $C_t/C_0 = 0.29$. These cobaltic catalysts could decompose MPS to degrade DHPK; however, the DHPK degradation efficiencies of Co₃O₄ NP and NCCo were noticeably lower than those of NCCF.

The pseudo 1st order equation was then used to quantitatively compare the performance of these catalysts for DHPK degradation, and the rate constants for DHPK degradation are summarized in Fig. 5(b). The rate constant (k) for NCCF + MPS would be 0.113 min^{-1} , which

was greater than the rate constants for Co₃O₄ NP + MPS (0.030 min^{-1}) and NCCo + MPS (0.064 min^{-1}), indicating that NCCF was superior to Co₃O₄ NP and NCCo.

Given that NCCF degraded DHPK much more rapidly than other catalysts, it would be intriguing to investigate MPS consumption by NCCF in comparison to other catalysts. In Fig. 5(c), the variation of MPS concentration during DHPK degradation was analyzed. In 30 min, 75% of MPS was degraded by NCCF during DHPK degradation, resulting in a precipitous decrease in MPS concentration. In contrast, MPS consumption during DHPK degradation by NCCo appeared significantly lower (~52%) and more sluggish. The rate constants of MPS consumption by these catalysts are displayed in Fig. 5(d), and the k using NCCF was determined to be 0.064 min^{-1} , while the rate constant by NCCo would be much smaller at 0.034 min^{-1} and that by Co₃O₄ NP was 0.014 min^{-1} , validating that the MPS consumption by NCCF appeared to be significantly more effective and faster than NCCo and Co₃O₄ NP, thereby allowing for the faster DHPK degradation.

Since activation of MPS involves surface reactions between MPS and catalysts, the surface chemistry of catalysts would play a crucial role in MPS activation [34]. As NCCF exhibited significantly greater catalytic activity for MPS activation, it would be prudent to compare the surface chemistry of these catalysts. As shown in Fig. 6, X-ray photoelectron spectroscopy (XPS) analyses of NCCF and NCCo were performed here. Specifically, the C1s curve of NCCF (Fig. 4(a)) would be resolved into multiple bands at 284.0, 286.6 and 288.5 eV, that correspond to the C–C, C–N, and C=O groups [35]. Additionally, the Co2p band of NCCF would be obtained and separated into distinct bands (Fig. 6(b)). Specifically, the band at 778.6 eV corresponds to Co⁰, while the bands at

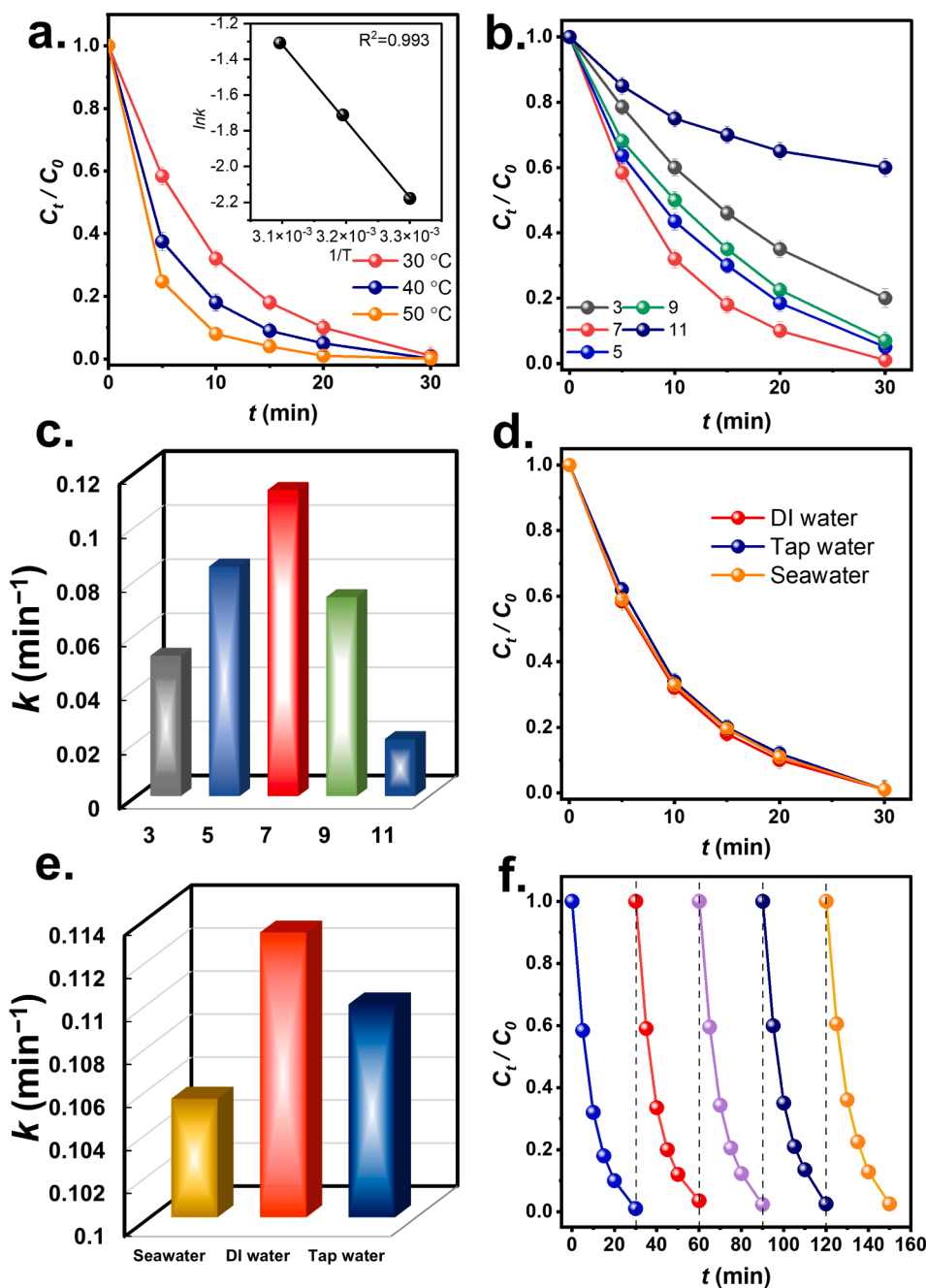


Fig. 10. Effects of various factors on DHPK degradation by NCCF + MPS: (a) temperature, (b,c) pH and corresponding rate constants, (d,e) water matrices; and (f) recyclability.

780.4 and 796.3 eV correspond to Co^{2+} species [36].

The band at 705.8 eV corresponds to Fe^0 in CoFe alloy [37]; 710.2, 713.4, and 723.3 eV could be Fe^{2+} and Fe^{3+} species, as CoFe NPs may be oxidized upon contact with oxygen. In addition, Fig. 6(d) reveals N1s in NCCF as multiple bands at 398.3, 399.4, 400.5 and 402.5 eV, corresponding to the pyridinic N, pyrrolic N, quaternary N, and N–O group [38].

Fig. S4 depicts the XPS analysis of NCCo for comparative purposes. Analysis of the C1s band revealed a series of bands corresponding to C–C, C–N, and C=O [35]. In addition, the band at 778.5 eV was related to Co^0 , but the bands at 780.2 and 796.3 eV corresponded to Co^{2+} [36]. The N1s band had numerous bands at 398.3, 399.4, 400.5 and 402.5 eV, corresponding to pyridinic N, pyrrolic N, quaternary N, and the N–O group, respectively [38].

According to previous findings, dual or multiple metallic compositions would provide additional reactive sites for mediating MPS activation [39], hence boosting catalytic activity. While both NCCF and NCCo contained Co species, NCCF was additionally composed of Fe^0 , Fe^{2+} and Fe^{3+} , that would serve as extra reactive sites for activating MPS [39,40].

Moreover, NCCF displayed a distinct pattern for nitrogenous species, with pyridinic N, pyrrolic N, and quaternary N contributing 60.9%, 29.2%, and 9.9%, respectively, while NCCo was composed of pyridinic N, pyrrolic N, and quaternary N as 58.2%, 27.7%, and 14.1%, respectively. Since both pyridinic N and pyrrolic N have been proven as active sites for MPS activation [41], the total quantity of pyridinic N and pyrrolic N in NCCF (i.e., 90.1%) was much higher than in NCCo (85.9%). It was hypothesized that the very high pyridinic and pyrrolic N

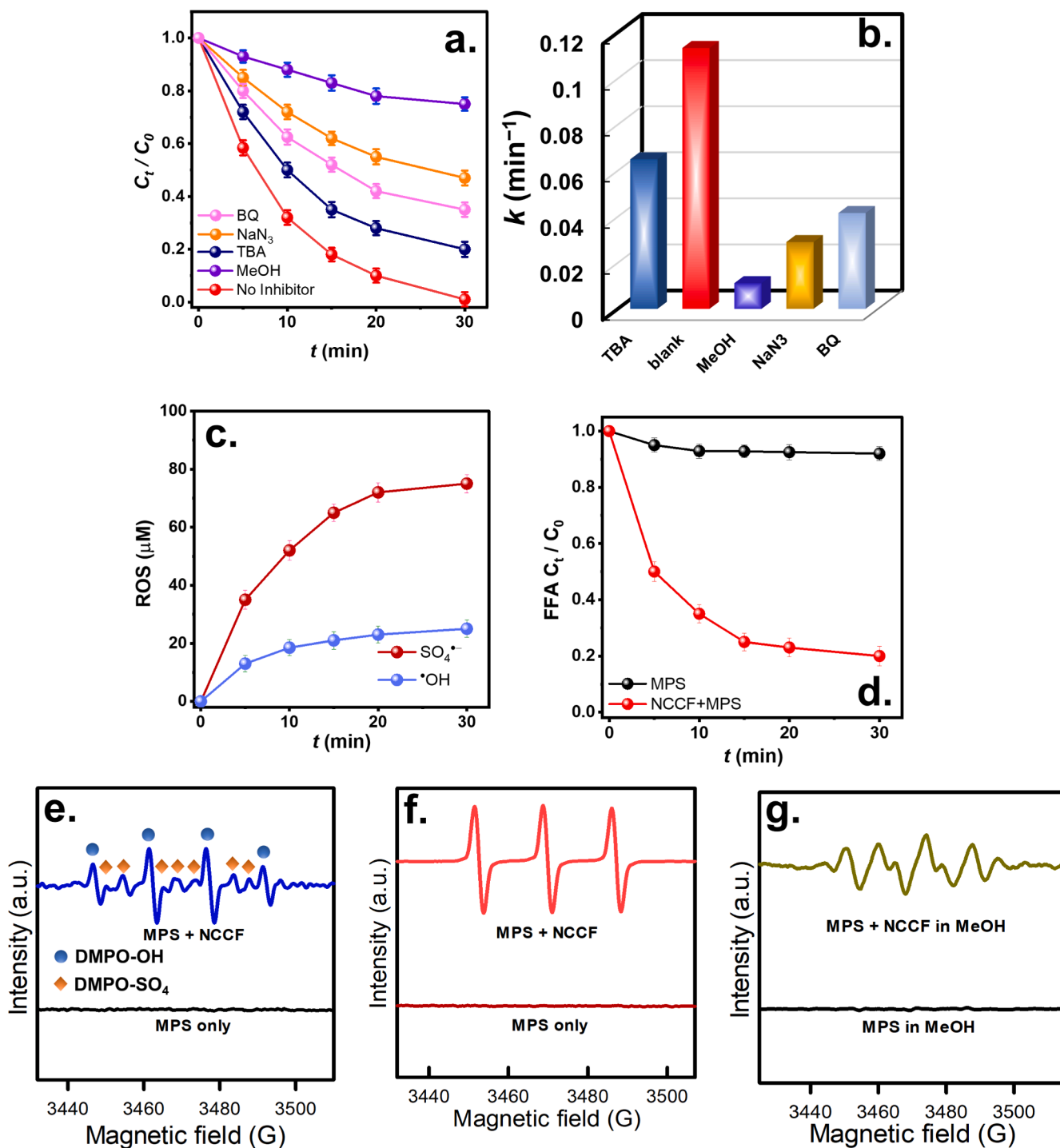


Fig. 11. (a–b) effects of scavengers on DHPK degradation; (c) the formation of $\text{SO}_4^{\bullet-}$ and $\bullet\text{OH}$ radicals; (d) FFA consumption; EPR analyses: (e) DMPO, (f) DMPO in methanol, (g) TEMP.

fractions in NCCF would enable NCCF to have many more active sites than NCCo, making NCCF possess stronger activities for activating MPS in DHPK decomposition.

In addition to XPS investigations, Raman spectroscopy was used to study the chemical distinctions between NCCF and NCCo by deciphering their structural fingerprints. Fig. 7(a) depicts the Raman spectra of NCCF and NCCo, both exhibit comparable patterns with peaks at 190, 470, and 680 cm^{-1} , which are ascribed to the F_{2g} , E_g , and A_{1g} vibration modes in Co metal species [42]. While these data demonstrate that both NCCF and NCCo were composed of Co, the magnified images of these

bands indicate distinct variances. For example, the band center of NCCo was 194 cm^{-1} , but the band center of NCCF's F_{2g} band changed to 186 cm^{-1} . Similar band shifts were seen in the case of A_{1g} . As the A_{1g} band of NCCo was centered at 677 cm^{-1} , and the center of the band in NCCF had shifted from 677 to 671 cm^{-1} . Since A_{1g} and F_{2g} might be attributed to the coordination of Co species, these changes implied that the NCCF included defected sites or oxygen vacancies [43]. This property may allow NCCF to expose more catalytically active surfaces [43], that enhance the catalytic activities of MPS activation.

On the other hand, MPS activation would also entail

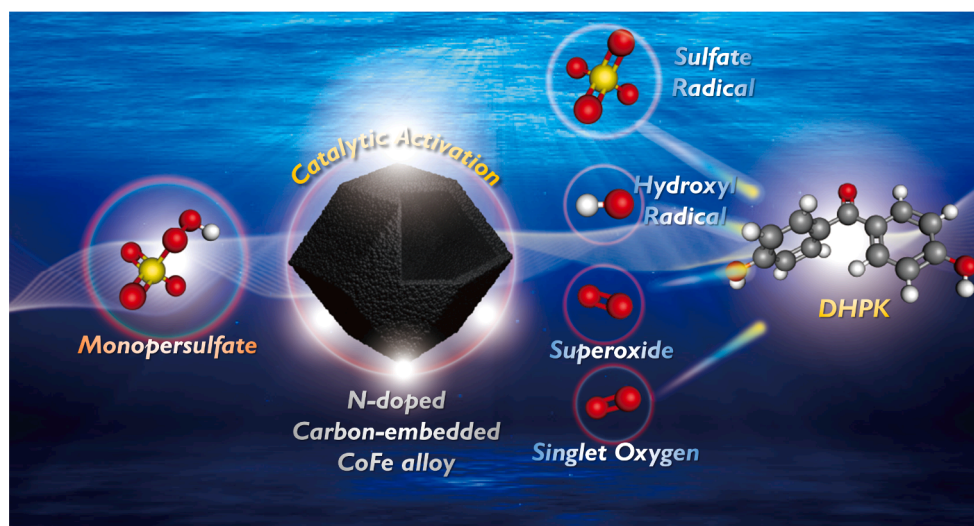


Fig. 12. A mechanistic illustration for DHPK degradation by NCCF-activated MPS.

reduction–oxidation processes in MPS and activators; as a result, electrochemistry of catalysts would also play a vital role in MPS activation [34]. As NCCF demonstrated much higher DHPK degradation activity than NCCo, it was instructive to investigate electrochemical differences between NCCF and NCCo. Fig. 8(a) depicts the cyclic voltammetry (CV) curves of NCCF and NCCo. In this potential window, NCCo presented a comparatively modest CV curve with less pronounced redox peaks, while NCCF displayed a noticeably bigger CV curve with pronounced redox peaks. NCCF displayed a significantly high specific capacitance of 21.6F/g compared to that of NCCo as 3.4F/g, indicating that NCCF had much better redox characteristics and would result in quicker interfacial processes [44].

In addition, the linear sweep voltammogram (LSV) curves of NCCF would be determined in Fig. 8(b). At 1000 μA , NCCF required a beginning potential of 0.72 V, whereas NCCo required a slightly higher starting potential of 0.94 V, indicating that the electrical transport in NCCF seemed to be more efficient than in NCCo. In addition, the charge transfers in both catalysts were studied using their respective Nyquist plots (Fig. 8(c)). Compared to NCCo, NCCF exhibited a much narrower semi-circle in the high-frequency region, suggesting that NCCF had a higher degree of charge transfer and a lower resistance [45]. These findings revealed that NCCF with improved porosity characteristics and more active surfaces would exhibit more favorable electrochemical behaviors, resulting in a much greater catalytic activity for MPS activation to destroy DHPK.

In addition, the distinction between NCCF and NCCo was uncovered by investigating the interactions of MPS with the active sites of NCCF and NCCo. The essential reactions (i.e. adsorption) between MPS and CoFe alloy in NCCF and Co in NCCo, respectively, were then investigated by computer-assisted investigation based on the Density Function Theory. Specifically, the geometrically-optimized (110) dominant plane of CoFe alloy in NCCF would be exhibited as a surface plane of CoFe, while the geometrically-optimized (111) dominant plane of Co in NCCo would be adopted as the surface of Co, as depicted in Fig. 9(b). The adsorption energy of MPS to the catalyst surface was quantified using the following equation (2):

$$\text{Adsorption energy}(E_{\text{adsorption}}) = E_{\text{MPS@catalyst}} - E_{\text{MPS}} - E_{\text{catalyst}} \quad (2)$$

The corresponding $E_{\text{adsorption}}$ of MPS to CoFe alloy at the (110) plane would be calculated as -1.7 eV, whereas $E_{\text{adsorption}}$ of MPS to Co alloy at the (111) plane was -1.2 eV. As the both cases of $E_{\text{adsorption}}$ were negative, MPS was validated to favorably adsorbed to these metallic surfaces. However, the more negative $E_{\text{adsorption}}$ in the case of CoFe alloy suggested that the adsorption of MPS onto NCCF might be more

favorable than that to NCCo. Such a difference might be also a factor for making NCCF exhibit the higher catalytic activity of MPS activation than NCCo.

3.3. Other factors on degradation of DHPK by NCCF + MPS system

Since NCCF + MPS was capable of removing DHPK from water, it was necessary to explore additional parameters, such as temperature and pH, that influence DHPK decomposition. Fig. 10(a) depicts DHPK eradication by NCCF + MPS at 30 to 50 °C. At 40 °C, the rate constant for DHPK elimination increased from 0.113 min^{-1} to 0.181 min^{-1} , allowing for substantially quicker removal. As the temperature increased to 50 °C, the rate of DHPK degradation increased to 0.270 min^{-1} , suggesting the beneficial impact of higher temperatures on DHPK elimination, presumably due to the enhanced mass transfer at higher temperatures. Moreover, the k values at different temperatures were modeled via the following law:

$$\ln k = \ln A - \frac{E_a}{RT} \quad (3)$$

The corresponding activation energy (E_a) was found to be 35.4 kJ/mol, which was more than several activation energy (E_a) values of degradation of UV stabilizers by sulfate-radical-based AOPs (Table S1), indicating that NCCF would be an advantageous activator for MPS to remove DHPK.

In Fig. 10(b), the effect of pH on DHPK removal by NCCF + MPS would be analyzed. At pH = 7, the neutral state, DHPK could be eliminated rapidly, however at pH = 5, the acidic condition, the rate of DHPK degradation slowed to 0.085 min^{-1} . Once the starting environment became more acidic, with a pH of 3, DHPK degradation further slowed with a k of 0.052 min^{-1} . The comparatively high concentration of H^+ in an acidic environment may interact with $\text{SO}_4^{\bullet-}$ as well as $\bullet\text{OH}$ to “consume” these radicals through the following equations: [46]:



Therefore, fewer radicals would be present in an acidic environment for DHPK degradation, resulting in a less efficient DHPK degradation. In addition, MPS itself would be more sluggish in acidic conditions [47], making MPS activation more difficult and subsequently resulting in less effective DHPK decomposition.

As the initial pH was 9, an alkaline state, DHPK degradation was significantly slowed, with a rate constant of $k = 0.074 \text{ min}^{-1}$. When the

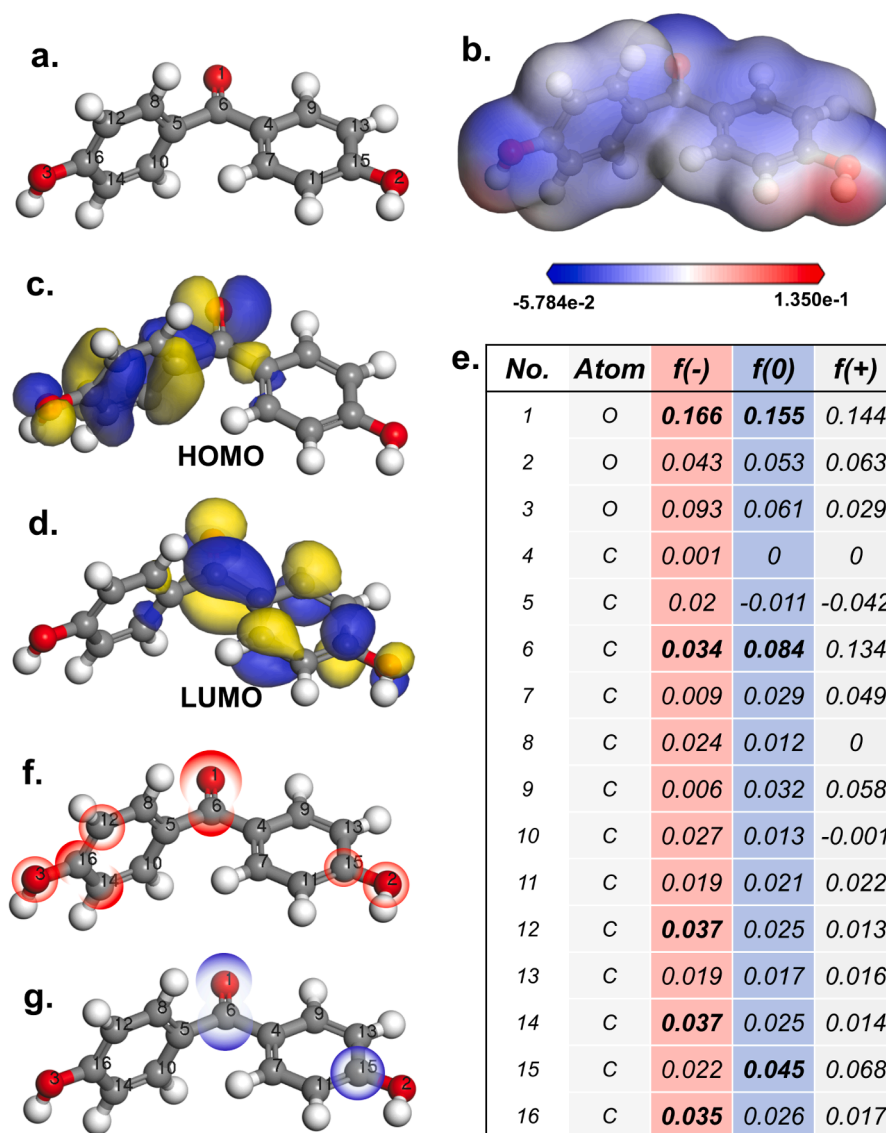


Fig. 13. DFT calculation for DHPK: (a) the optimized molecule structure, (b) HOMO; (c) LUMO, (d) electrostatic potential (ESP); (e) a summary of Fukui indices; major sites of Fukui index for (f) electrophilic attack (f^+), and (g) radical attack (f^0).

pH was increased to 11, the rate of DHPK degradation reduced to $k = 0.021 \text{ min}^{-1}$. The data also indicate that the alkaline condition appeared slightly unfavorable for DHPK degradation by NCCF + MPS, possibly because the NCCF surface may become more negatively charged in a basic environment, resulting in a stronger repulsion between DHPK, NCCF, and SO_5^{2-} and limiting radical production [48]. In addition, given that the pK_a of MPS is 9.4, the extremely basic state would intensify the electrostatic repulsion, hence limiting the interaction between MPS and NCCF [47].

Moreover, it would be interesting to further investigate DHPK decomposition by NCCF + MPS in different water conditions. In addition to DI water, tap water and seawater containing DHPK were used as testing media in Fig. 10(d). Notably, the commencement of DHPK degradation with a rate constant of $k = 0.110 \text{ min}^{-1}$ was still very efficient when tap water was employed. Since tap water includes several chemicals, such as ions and particulates, the overall effectiveness of DHPK degradation was still satisfactory, as DHPK was completely removed after 30 min. Despite the slightly lowered k value of 0.106 min^{-1} , DHPK might still be removed by NCCF + MPS in seawater because seawater contains a large quantity of contaminants, mainly ions

and minerals.

It was probable that Cl^- is present in seawater and tap water, which contributes to their less effective degradation because Cl^- may react with $\text{SO}_4^{\cdot-}$ to produce chloride radicals (i.e., Cl^{\cdot} , $\text{Cl}_2^{\cdot-}$) [49], which have less oxidation power than $\text{SO}_4^{\cdot-}$; hence, the DHPK elimination efficiency fell. NCCF + MPS remained an efficient and practical approach for degrading DHPK in both potable and marine media.

3.4. Recyclability of NCCF for DHPK elimination

As NCCF activated MPS to effectively DHPK, the potential of NCCF to remove MPS across several cycles was investigated. Fig. 10(f) illustrates that NCCF was able to degrade DHPK throughout 5 continuous cycles without substantial decreases. This information indicates that the spent NCCF remained stable and advantageous for activating MPS in DHPK degradation. In Fig. S5, the XRD pattern of spent NCCF was compared to that of pure NCCF, suggesting that NCCF was a stable and robust heterogeneous catalyst.

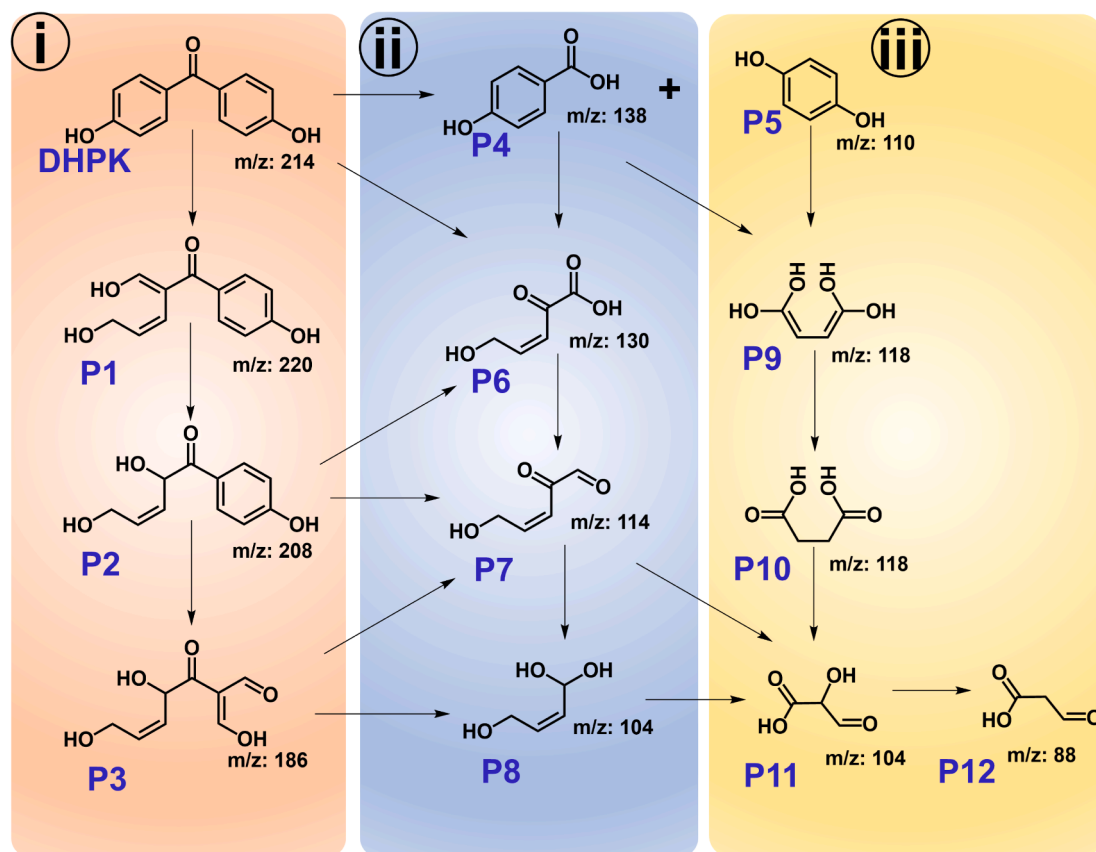


Fig. 14. A proposed degradation process of DHPK based on the detected intermediates.

3.5. Degradation mechanism by NCCF + MPS

Then, a series of probe agents would be studied to better understand the ROS types implicated in DHPK degradation. *Tert*-butanol (TBA) would be utilized as a probe agent for $\cdot\text{OH}$, whereas methanol can be employed to detect $\text{SO}_4^{\cdot-}$ and $\cdot\text{OH}$. When TBA was added, DHPK degradation progressed significantly more slowly, and the rate constant reduced from 0.113 to 0.065 min^{-1} , indicating that $\cdot\text{OH}$ is present and contributes to DHPK degradation (Fig. 11(a)). When methanol was added, the DHPK degradation seemed to be severely impeded, as its k was only 0.011 min^{-1} , indicating that $\text{SO}_4^{\cdot-}$ and $\cdot\text{OH}$ would coexist during DHPK degradation. In addition, another probe agent, benzoquinone (BQ), was used to assess the presence of superoxide ($\text{O}_2^{\cdot-}$). Fig. 11 (b) demonstrates that the addition of BQ slowed DHPK degradation to a rate of $k = 0.042 \text{ min}^{-1}$, showing that $\text{O}_2^{\cdot-}$ may also be produced during DHPK degradation. In addition, another probe agent, NaN_3 , was used to investigate the presence of the non-radical species, singlet oxygen ($^1\text{O}_2$), and the addition of NaN_3 slowed down the rate of DHPK degradation with a $k = 0.029 \text{ min}^{-1}$, indicating that $^1\text{O}_2$ may have been produced from NCCF + MPS during DHPK degradation, implicating the non-radical decomposition pathway.

The generation of $\text{SO}_4^{\cdot-}$ and $\cdot\text{OH}$ at different intervals would be calculated using “semi-quantitative” research utilizing specialized probe agents [50,51] to study the occurrence of such ROS in further detail. As shown in Fig. 11(c), the production of *para*-benzoquinone (*p*-BQ) and *para*-hydroxybenzoic acid (*p*-HPA) verified the presence of $\text{SO}_4^{\cdot-}$ and $\cdot\text{OH}$, showing that the concentrations of $\text{SO}_4^{\cdot-}$ and $\cdot\text{OH}$ rose with time. However, it seemed that the amount of $\text{SO}_4^{\cdot-}$ was larger than that of $\cdot\text{OH}$, which was consistent to the aforementioned result using the probe agents.

In addition, the production of $^1\text{O}_2$ could be determined by linking it to the furfuryl alcohol (FFA) consumed during the reaction with $^1\text{O}_2$

[52]. Fig. 11(d) depicts the FFA consumption at various reaction periods for MPS alone and NCCF + MPS. One can observe that MPS without NCCF would result in marginal production of $^1\text{O}_2$. However, NCCF + MPS would accelerate the consumption of FFA, corroborating that NCCF would lead to the decomposition of MPS and initiate the generation of $^1\text{O}_2$ for the non-radical destruction of DHPK.

Using 5,5-Dimethyl-1-pyrroline *N*-oxide (DMPO) and 2,2,6,6-tetramethylpiperidine (TEMP) as spin-trapping agents, electron paramagnetic resonance (EPR) would then be used to detect the actual species of ROS produced by NCCF + MPS during DHPK breakdown. No clear trend was found when DMPO was injected in the absence of NCCF, as shown in Fig. 11(e). As DMPO, MPS, and NCCF were present concurrently, however, a different pattern was found and ascribed to DMPO- SO_4 and DMPO-OH, as shown in Fig. 11(e). This establishes that $\text{SO}_4^{\cdot-}$ and $\cdot\text{OH}$ might be formed by MPS + NCCF, hence contributing to DHPK degradation. In addition, the same experiment was conducted in methanol to see whether superoxide (Fig. 11(f)), $\text{O}_2^{\cdot-}$, would be created from NCCF + MPS, and a significant signal was obtained and accurately attributed to DMPO- O_2 , confirming the presence of $\text{O}_2^{\cdot-}$.

In contrast, when the trapping agent TEMP was used, essentially no detectable signal was seen for TEMP and MPS. Once TEMP, MPS, and NCCF were administered together, however, a unique triplet pattern was detected and attributed to TEMP- $^1\text{O}_2$ (Fig. 11(g)), proving that $^1\text{O}_2$ existed and contributed to DHPK degradation through the non-radical route. These investigations further confirmed that DHPK degradation by NCCF + MPS entailed a number of ROS ($\text{SO}_4^{\cdot-}$, $\cdot\text{OH}$, $\text{O}_2^{\cdot-}$, $^1\text{O}_2$) as illustrated in Fig. 12.

3.6. Degradation pathway of DHPK by NCCF and MPS

Since NCCF may effectively activate MPS to degrade DHPK, it was necessary to further examine the DHPK elimination pathway. Recently,

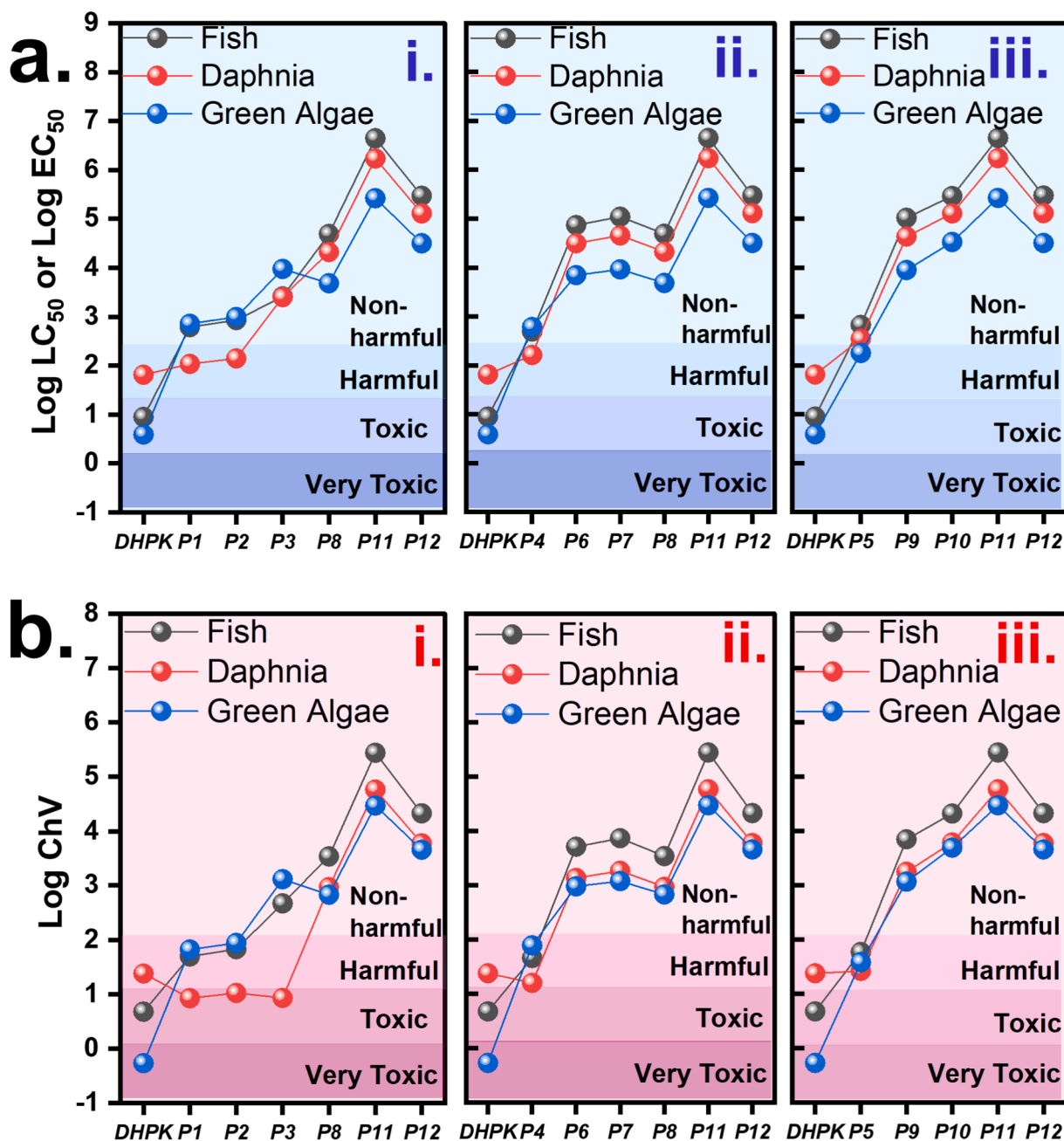


Fig. 15. Eco-toxicity evaluation of DHPK degradation by the ECOSAR: (a) acute toxicities; (b) chronic toxicities.

with advance of computational power, quantum chemistry computation approaches (QCC) has been reported for reaction pathways, kinetics and regioselectivity [53]. Therefore, to explore the DHPK degradation process by ROS, the molecular susceptibility of DHPK was analyzed using computational chemistry and the Density Functional Theory (DFT). As demonstrated in Fig. 13(a), the molecular structure of DHPK was geometrically optimized. Consequently, Fig. 13(c) and (d) depict DHPK's highest occupied molecular orbital (HOMO) and lowest unoccupied molecular orbital (LUMO). According to the literature [53], interactions between molecular structures and radicals can be also forecasted to further understand degradation mechanisms. In general, HOMO regions would be susceptible to electrophilic assaults, and both $\text{SO}_4^{\bullet-}$ and $^{\bullet}\text{OH}$ are thought to be electrophilic, as is $^1\text{O}_2$, which is a highly electrophilic molecule. Consequently, the HOMO at the benzene ring of

DHPK seemed susceptible to electrophilic assaults from these ROS. Fig. 13(b) depicts the electrostatic potential-mapped isosurface of DHPK, indicating that the electron-rich area (the blue-colored zones) of DHPK would be susceptible to electrophilic processes.

The Fukui indices of DHPK were then calculated and presented in Fig. 13(e) in order to differentiate the possible region of DHPK for acquiring attacks. Specifically, f^- , f^0 , and f^+ indicate the electrophilic, radical, and nucleophilic attacks, respectively. Due to the fact that $^1\text{O}_2$ is a highly reactive electrophilic molecule, DHPK sites with relatively high and positive f^- values are more susceptible to electrophilic assaults. In particular, 10, 6C, 12C, 14C, and 16C exhibit rather high f^- values, indicating that these sites are susceptible to electrophilic attacks (as seen in Fig. 13(f)). However, since 10 would be saturated, 12C, 14C, and 16C were other potential locations for first strikes. Moreover, sites with high

f^0 values are more sensitive to radical attacks; similarly, 6C and 15C may be more susceptible to radical attacks during DHPK degradation by NCCF + MPS (as seen in Fig. 13(g)).

To evaluate the decomposition route of DHPK by NCCF + MPS, the mass spectrometry of DHPK degradation products (Fig. S6 and Table S2) was studied and integrated with the above-mentioned theoretical information to suggest the degradation process shown in Fig. 14. Initially, the benzene ring of DHPK, where the HOMO resides, would be subjected to a ring-opening attack to form an intermediate, P1, which would subsequently be degraded to yield P2. In response to the continual ring-opening reaction, P2 would disintegrate further to produce P3.

On the other hand, DHPK may be first degraded by splitting it into two pieces by the routes (ii) and (iii), yielding the byproducts P4 and P5. Next, P4 would undergo the ring-opening reaction to generate P6, which is then constantly degraded to generate P7 and P8 in succession. Alternately, P5 would be degraded by a second ring-opening assault to produce P9, which is then progressively dissolved into P10, P11, and P12.

3.7. Eco-toxicity evaluation of DHPK degradation intermediates

Based on the decomposition process of DHPK by NCCF + MPS, it was also crucial to evaluate the eco-toxicity of intermediates generated from DHPK elimination particularly for aquatic ecology. Herein, the Ecological Structure Activity Relationships (ECOSAR) Predictive Model is then adopted here to examine variations in toxicity of degradation intermediates from DHPK based on acute toxicity ($LC_{50}^{\text{fish/daphnia}}$ & $EC_{50}^{\text{green algae}}$) and chronic toxicity ($ChV^{\text{fish/daphnia/green algae}}$) as shown in Fig. 15 (a) and (b), respectively. Based on the Globally Harmonized System of Classification and Labelling of Chemicals (Table S3), the data of LC_{50} of these intermediates from the ECOSAR could be then categorized into the four levels of toxicity (i.e., very toxic, toxic, harmful and non-harmful). Fig. 15(a) and (b) display values of these intermediates as well as their categories. Initially, the toxicity of pristine DHPK was relatively high (i.e., very low dosage of LC_{50} or EC_{50}). As DHPK was decomposed, the toxicities of the initial intermediates (P1 and P2) seemed to decrease gradually for fish, daphnia as well as algae, and then toxicities were significantly reduced after the degradation in P3 ~ P12. The similar trends can be also observed in the case of chronic toxicities in Fig. 15(b) as the initial chronic toxicities (Log ChV) was extremely low as a result of high toxicities; however, after the degradation process, the values of Log ChV increased significantly for fish, daphnia as well as algae, indicating that the degradation process would substantially lower the toxicities and transfer the toxic DHPK into less-toxic (even non-harmful) by-products.

4. Conclusion

NCCF was proposed and facilely constructed to demonstrate a unique hollow-engineered nanostructure and the composition of CoFe alloy by employing Co-ZIF as a precursor after the easy etching and Fe doping procedures in order to build a promising heterogeneous catalyst to activate MPS. The Fe dopant encapsulated CoFe alloy NPs inside a hollow-structured N-doped carbon matrix, allowing NCCF to exhibit increased meso-porosity, active N species, and improved electrochemical characteristics compared to NCCo, its analogue without Fe dopants. NCCF showed a much higher magnetization of 82.5 emu/g, and much more activity (with a $k = 0.113 \text{ min}^{-1}$) than NCCo (with a $k = 0.064 \text{ min}^{-1}$) and the standard catalyst, Co_3O_4 NP, for the activation of MPS to degrade DHPK. In addition, NCCF + MPS demonstrated an even lower activation energy (E_a) of 35.4 kJ/mol for DHPK degradation compared to the literature and maintained its excellent efficacy in removing DHPK in various water environments. NCCF also maintained its composition and activity across the consecutive five cycles of degradation. The mechanism of DHPK degradation has been detailedly studied, and both radical and non-radical pathways have been uncovered. In agreement with the ecotoxicity evaluation, the degradation of DHPK by NCCF +

MPS did not result in the generation of hazardous or severely toxic metabolites (with $LC_{50} > 100 \text{ mg/L}$). This renders NCCF a suitable heterogeneous catalyst for MPS activation to degrade DHPK and other emerging contaminants.

CRedit authorship contribution statement

Tran Doan Trang: Data curation, Writing – original draft. **Jechan Lee:** Writing – original draft. **Wen-Da Oh:** Data curation, Visualization, Investigation. **Eilhann Kwon:** Data curation. **Haitao Wang:** . **Yiu Fai Tsang:** Data curation. **Venkata Subbaiah Munagapati:** Visualization. **Hongta Yang:** Writing – original draft. **Wei-Hsin Chen:** Investigation. **Kun-Yi Andrew Lin:** Writing – original draft.

Declaration of Competing Interest

The authors declare that they have no known competing financial interests or personal relationships that could have appeared to influence the work reported in this paper.

Data availability

The authors are unable or have chosen not to specify which data has been used.

Appendix A. Supplementary data

Supplementary data to this article can be found online at <https://doi.org/10.1016/j.jcis.2023.08.091>.

References

- [1] A. Hassani, P. Eghbali, F. Mahdipour, S. Wacławek, K.-Y.-A. Lin, F. Ghanbari, Insights into the synergistic role of photocatalytic activation of peroxymonosulfate by UVA-LED irradiation over CoFe2O4-rGO nanocomposite towards effective Bisphenol A degradation: Performance, mineralization, and activation mechanism, *Chem. Eng. J.* 453 (2023) 139556.
- [2] Z.Y. Choong, K.Y.A. Lin, G. Lisak, T.T. Lim, W.D. Oh, Multi-heteroatom-doped carbocatalyst as peroxymonosulfate and peroxydisulfate activator for water purification: A critical review, *J. Hazard. Mater.* 426 (2022).
- [3] S. Giannakis, K.-Y.-A. Lin, F. Ghanbari, A review of the recent advances on the treatment of industrial wastewaters by sulfate radical-based advanced oxidation processes (SR-AOPs), *Chem. Eng. J.* 406 (2021) 127083.
- [4] S.Y. Yang, P. Wang, X. Yang, L. Shan, W.Y. Zhang, X.T. Shao, R. Niu, Degradation efficiencies of azo dye Acid Orange 7 by the interaction of heat, UV and anions with common oxidants: Persulfate, peroxymonosulfate and hydrogen peroxide, *J. Hazard. Mater.* 179 (2010) 552–558.
- [5] B.-T. Zhang, W. Xiang, X. Jiang, Y. Zhang, Y. Teng, Oxidation of Dyes by Alkaline-Activated Peroxymonosulfate, *J. Environ. Eng.* 142 (4) (2016).
- [6] G.L. Wei, X.L. Liang, Z.S. He, Y.S. Liao, Z.Y. Xie, P. Liu, S.C. Ji, H.P. He, D.Q. Li, J. Zhang, Heterogeneous activation of Oxone by substituted magnetites Fe₃-xMxO₄ (Cr, Mn Co, Ni) for degradation of Acid Orange II at neutral pH, *J. Mol. Catal. A-Chem* 398 (2015) 86–94.
- [7] C. Cai, H. Zhang, X. Zhong, L. Hou, Ultrasound enhanced heterogeneous activation of peroxymonosulfate by a bimetallic Fe–Co/SBA-15 catalyst for the degradation of Orange II in water, *J. Hazard. Mater.* 283 (2015) 70–79.
- [8] X. Yang, X. Xie, S. Li, W. Zhang, X. Zhang, H. Chai, Y. Huang, The POM@MOF hybrid derived hierarchical hollow Mo/Co bimetal oxides nanocages for efficiently activating peroxymonosulfate to degrade levofloxacin, *J. Hazard. Mater.* 419 (2021) 126360.
- [9] Q. Chen, Y. Liu, Y. Lu, Y. Hou, X. Zhang, W. Shi, Y. Huang, Atomically dispersed Fe/Be dual active sites single-atom nanozymes for cascade catalysis and peroxymonosulfate activation to degrade dyes, *J. Hazard. Mater.* 422 (2022) 126929.
- [10] W.-J. Liu, Y.-K. Park, H.M. Bui, N.N. Huy, C.-H. Lin, S. Ghotekar, T. Wi-Afedzi, K.-Y. Lin, Hofmann-MOF-derived CoFeNi nanoalloy@CNT as a magnetic activator for peroxymonosulfate to degrade benzophenone-I in water, *J. Alloy. Compd.* 937 (2023) 165189.
- [11] J. Wu, X. Yan, W. Wang, M. Jin, Y. Xie, C. Wang, Highly dispersed CoNi alloy embedded in N-doped graphitic carbon for catalytic transfer hydrogenation of biomass-derived furfural, *Chemistry – An Asian Journal* 16 (2021) 3194–3201.
- [12] H. Li, S. Lu, J. Zheng, N. Li, Y. Lou, J. Tang, J. Zhou, H. Zhang, M. Huang, D. Wang, MOFs-derived hollow FeCo@C as peroxymonosulfate activator for degradation of organic pollutants: Insight into the catalytic sites by experimental and theoretical study, *Sep. Purif. Technol.* 299 (2022) 121779.

- [13] W.-J. Liu, Y.-K. Park, H.M. Bui, N.N. Huy, C.-H. Lin, S. Ghotekar, T. Wi-Afedzi, K.-Y.-A. Lin, Hofmann-MOF-derived CoFeNi nanoalloy@CNT as a magnetic activator for peroxymonosulfate to degrade benzophenone-1 in water, *J. Alloy. Compd.* 937 (2023) 165189.
- [14] W.-J. Liu, E. Kwon, B. Xuan Thanh, T. Cong Khiem, D. Dinh Tuan, J.-Y. Lin, T. Wi-Afedzi, C. Hu, S. Sirivithayapakorn, K.-Y.-A. Lin, Hofmann-MOF derived nanoball assembled by FeNi alloy confined in carbon nanotubes as a magnetic catalyst for activating peroxydisulfate to degrade an ionic liquid, *Sep. Purif. Technol.* 295 (2022) 120945.
- [15] W.-J. Liu, E. Kwon, B.X. Thanh, J. Lee, C.K. Ta, S. Sirivithayapakorn, K.-Y.-A. Lin, Nanoscale CoNi alloy@ carbon derived from Hofmann-MOF as a magnetic/effective activator for monopersulfate to eliminate an ultraviolet filter, *Journal of Nanostructure in Chemistry* (2022) 1–14.
- [16] L. Hu, R. Zhang, L. Wei, F. Zhang, Q. Chen, Synthesis of FeCo nanocrystals encapsulated in nitrogen-doped graphene layers for use as highly efficient catalysts for reduction reactions, *Nanoscale* 7 (2) (2015) 450–454.
- [17] Y. Deng, X.i. Zou, Z. Liu, J. Wang, Z. Wang, J. Tang, Co7Fe3/CoFe2O4@C lamellar composites derived from Co-Fe LDH/PVA as an effective heterogeneous activator of peroxymonosulfate, *J. Alloy. Compd.* 854 (2021) 157244.
- [18] P. Shukla, H. Sun, S. Wang, H.M. Ang, M.O. Tadé, Nanosized Co3O4/SiO2 for heterogeneous oxidation of phenolic contaminants in waste water, *Sep. Purif. Technol.* 77 (2) (2011) 230–236.
- [19] Y. Yao, Z. Yang, H. Sun, S. Wang, Hydrothermal synthesis of Co3O4-graphene for heterogeneous activation of peroxymonosulfate for decomposition of phenol, *Ind. Eng. Chem. Res.* 51 (46) (2012) 14958–14965.
- [20] W.J. Ma, N. Wang, Y.C. Du, T.Z. Tong, L.J. Zhang, K.Y.A. Lin, X.J. Han, One-step synthesis of novel Fe3C@nitrogen-doped carbon nanotubes/graphene nanosheets for catalytic degradation of Bisphenol A in the presence of peroxymonosulfate, *Chem. Eng. J.* 356 (2019) 1022–1031.
- [21] N.a. Wang, W. Ma, Z. Ren, Y. Du, P. Xu, X. Han, Prussian blue analogues derived porous nitrogen-doped carbon microspheres as high-performance metal-free peroxymonosulfate activators for non-radical-dominated degradation of organic pollutants, *J. Mater. Chem. A* 6 (3) (2018) 884–895.
- [22] H.T. Nguyen, J. Lee, E. Kwon, G. Lisak, B.X. Thanh, F. Ghanbari, K.-Y. Lin, Bamboo-like N-doped carbon nanotube-confined cobalt as an efficient and robust catalyst for activating monopersulfate to degrade bisphenol A, *Chemosphere* 279 (2021) 130569.
- [23] X. Duan, H. Sun, Y. Wang, J. Kang, S. Wang, N-doping-induced nonradical reaction on single-walled carbon nanotubes for catalytic phenol oxidation, *ACS Catal.* 5 (2) (2015) 553–559.
- [24] H. Zhou, S. Wu, Y. Zhou, Y. Yang, J. Zhang, L. Luo, X. Duan, S. Wang, L. Wang, D.C. W. Tsang, Insights into the oxidation of organic contaminants by iron nanoparticles encapsulated within boron and nitrogen co-doped carbon nanoshell: Catalyzed Fenton-like reaction at natural pH, *Environ. Int.* 128 (2019) 77–88.
- [25] G. Zhou, L. Zhou, H. Sun, H.M. Ang, M.O. Tadé, S. Wang, Carbon microspheres supported cobalt catalysts for phenol oxidation with peroxymonosulfate, *Chem. Eng. Res. Des.* 101 (2015) 15–21.
- [26] S. Wu, J. Liu, H. Wang, H. Yan, A review of performance optimization of MOF-derived metal oxide as electrode materials for supercapacitors, *Int. J. Energy Res.* 43 (2019) 697–716.
- [27] J.Y. Lin, J. Lee, W.D. Oh, E. Kwon, Y.C. Tsai, G. Lisak, S. Phattarapattamawong, C. Hu, K.Y.A. Lin, Hierarchical ZIF-decorated nanoflower-covered 3-dimensional foam for enhanced catalytic reduction of nitrogen-containing contaminants, *J. Colloid Interface Sci.* 602 (2021) 95–104.
- [28] K.-Y.-A. Lin, H.-A. Chang, Zeolitic Imidazole framework-67 (ZIF-67) as a heterogeneous catalyst to activate peroxymonosulfate for degradation of Rhodamine B in water, *J. Taiwan Inst. Chem. Eng.* 53 (2015) 40–45.
- [29] A.N. Eddine, J.P. von Kries, M.V. Podust, T. Warrrier, S.H.E. Kaufmann, L. M. Podust, X-ray structure of 4,4'-dihydroxybenzophenone mimicking sterol substrate in the active site of sterol 14 α -demethylase (CYP51)*, *J. Biol. Chem.* 283 (2008) 15152–15159.
- [30] K.-Y. Lin, H.-A. Chang, Ultra-high adsorption capacity of zeolitic imidazole framework-67 (ZIF-67) for removal of malachite green from water, *Chemosphere* 139 (2015) 624–631.
- [31] D.D. Tuan, K.-Y.-A. Lin, Ruthenium supported on ZIF-67 as an enhanced catalyst for hydrogen generation from hydrolysis of sodium borohydride, *Chem. Eng. J.* 351 (2018) 48–55.
- [32] Z. Wu, L. Wang, S. Chen, X. Zhu, Q. Deng, J. Wang, Z. Zeng, S. Deng, Facile and low-temperature strategy to prepare hollow ZIF-8/CNT polyhedrons as high-performance lithium-sulfur cathodes, *Chem. Eng. J.* 404 (2021) 126579.
- [33] B. Tang, S. Li, W.-C. Song, Y. Li, E.-C. Yang, X.-J. Zhao, L. Li, Hollow Zn–Co based zeolitic imidazole framework as a robust heterogeneous catalyst for enhanced CO2 chemical fixation, *Chemistry – An Asian Journal* 14 (2019) 4375–4382.
- [34] W.-J. Liu, E. Kwon, N.N. Huy, T.C. Khiem, G. Lisak, T. Wi-Afedzi, C.-C. Wu, F. Ghanbari, K.-Y.-A. Lin, Facilely-prepared sulfide-doped Co3O4 nanocomposite as a boosted catalyst for activating Oxone to degrade a sunscreen agent, *J. Taiwan Inst. Chem. Eng.* 133 (2022) 104253.
- [35] G. Li, J.H. Sun, W.P. Hou, S.D. Jiang, Y. Huang, J.X. Geng, Three-dimensional porous carbon composites containing high sulfur nanoparticle content for high-performance lithium-sulfur batteries, *Nat. Commun.* 7 (2016).
- [36] Z. Hasan, D.W. Cho, C.M. Chon, K. Yoon, H. Song, Reduction of p-nitrophenol by magnetic Co-carbon composites derived from metal organic frameworks, *Chem. Eng. J.* 298 (2016) 183–190.
- [37] P. He, Y. Wu, H. Chen, Z. Zhu, H. Liu, J. Gao, H. Xu, Hierarchical bimetal embedded in carbon nanoflower electrocatalysts derived from metal-organic frameworks for efficient oxygen evolution reaction, *J. Alloy. Compd.* 813 (2020) 152192.
- [38] D.Y. Osadchii, A.I. Olivos-Suarez, A.V. Bavykina, J. Gascon, Revisiting nitrogen species in covalent triazine frameworks, *Langmuir* 33 (2017) 14278–14285.
- [39] X. Sun, H. Qi, S. Mao, Z. Sun, Atrazine removal by peroxymonosulfate activated with magnetic CoFe alloy@N-doped graphitic carbon encapsulated in chitosan carbonized microspheres, *Chem. Eng. J.* 423 (2021) 130169.
- [40] Z. Liu, X. Sun, Z. Sun, CoNi alloy anchored onto N-doped porous carbon for the removal of sulfamethoxazole: Catalyst, mechanism, toxicity analysis, and application, *Chemosphere* 308 (2022) 136291.
- [41] J. Miao, W. Geng, P.J.J. Alvarez, M. Long, 2D N-doped porous carbon derived from polydopamine-coated graphitic carbon nitride for efficient nonradical activation of peroxymonosulfate, *Environ. Sci. Tech.* 54 (13) (2020) 8473–8481.
- [42] Y. Wang, X. Wei, X. Hu, W. Zhou, Y. Zhao, Effect of formic acid treatment on the structure and catalytic activity of Co3O4 for N2O decomposition, *Catal. Lett.* 149 (4) (2019) 1026–1036.
- [43] Z. Wang, W. Wang, L. Zhang, D. Jiang, Surface oxygen vacancies on Co3O4 mediated catalytic formaldehyde oxidation at room temperature, *Catalysis, Sci. Technol.* 6 (11) (2016) 3845–3853.
- [44] T.C. Khiem, X. Duan, W.-J. Liu, Y.-K. Park, H.M. Bui, W.-D. Oh, S. Ghotekar, Y. F. Tsang, K.-Y. Lin, MOF-templated hollow cobalt sulfide as an enhanced oxone activator for degradation of UV absorber: Key role of sulfur vacancy-induced highly active coii sites, *Chem. Eng. J.* 453 (2023) 139699.
- [45] Y. Li, F.-M. Li, X.-Y. Meng, S.-N. Li, J.-H. Zeng, Y.u. Chen, Ultrathin Co3O4 nanomeses for the oxygen evolution reaction, *ACS Catal.* 8 (3) (2018) 1913–1920.
- [46] H.T. Nguyen, J. Lee, E. Kwon, G. Lisak, B.X. Thanh, W.D. Oh, K.-Y.-A. Lin, Metal-complexed covalent organic frameworks derived N-doped carbon nanobubble-embedded cobalt nanoparticle as a magnetic and efficient catalyst for oxone activation, *J. Colloid Interface Sci.* 591 (2021) 161–172.
- [47] W. Guo, S. Su, C. Yi, Z. Ma, Degradation of antibiotics amoxicillin by Co3O4-catalyzed peroxymonosulfate system, *Environ. Prog. Sustain. Energy* 32 (2013) 193–197.
- [48] D.D. Tuan, C. Khiem, E. Kwon, Y.F. Tsang, S. Sirivithayapakorn, B.X. Thanh, G. Lisak, H. Yang, K.-Y.-A. Lin, Hollow porous cobalt oxide nanobox as an enhanced for activating monopersulfate to degrade 2-hydroxybenzoic acid in water, *Chemosphere* 294 (2022) 133441.
- [49] T. Zhang, Y. Chen, Y. Wang, J. Le Roux, Y. Yang, J.-P. Croué, Efficient peroxydisulfate activation process not relying on sulfate radical generation for water pollutant degradation, *Environ. Sci. Tech.* 48 (2014) 5868–5875.
- [50] J.-Y. Yin, H. Wang, K.-P. Yu, J. Lee, K.-Y.-A. Lin, Degradation of sunscreen agent 2-phenylbenzimidazole-5-sulfonic acid using monopersulfate activated by MOF-derived cobalt sulfide nanoplates, *J. Water Process Eng.* 44 (2021) 102282.
- [51] T.C. Khiem, D.D. Tuan, E. Kwon, N.N. Huy, W.-D. Oh, W.-H. Chen, K.-Y.-A. Lin, Degradation of dihydroxybenzophenone through monopersulfate activation over nanostructured cobalt ferrites with various morphologies: A comparative study, *Chem. Eng. J.* 450 (2022) 137798.
- [52] S. Mostafa, F.L. Rosario-Ortiz, Singlet oxygen formation from wastewater organic matter, *Environ. Sci. Tech.* 47 (2013) 8179–8186.
- [53] S. Wacławek, Do we still need a laboratory to study advanced oxidation processes? A review of the modelling of radical reactions used for water treatment, *Ecol. Chem. Eng. S* 28 (1) (2021) 11–28.